Biomedical Optics EXPRESS

# Optical coherence tomography can assess skeletal muscle tissue from mouse models of muscular dystrophy by parametric imaging of the attenuation coefficient

**Blake R. Klyen,[1,*] Loretta Scolaro,[1] Tea Shavlakadze,[2] Miranda D. Grounds,[2] and David D. Sampson[1,3]**

[1]*Optical + Biomedical Engineering Laboratory, School of Electrical, Electronic and Computer Engineering, The University of Western Australia, M018, 35 Stirling Highway, Crawley, Western Australia 6009, Australia*
[2]*Skeletal Muscle Research Group, School of Anatomy, Physiology and Human Biology, The University of Western Australia, M309, 35 Stirling Highway, Crawley, Western Australia 6009, Australia*
[3]*Centre for Microscopy, Characterisation and Analysis, The University of Western Australia, M010, 35 Stirling Highway, Crawley, Western Australia 6009, Australia*
**klyenb01@student.uwa.edu.au*

**Abstract:** We present the assessment of *ex vivo* mouse muscle tissue by quantitative parametric imaging of the near-infrared attenuation coefficient $\mu_t$ using optical coherence tomography. The resulting values of the local total attenuation coefficient $\mu_t$ (mean ± standard error) from necrotic lesions in the dystrophic skeletal muscle tissue of *mdx* mice are higher (9.6 ± 0.3 $mm^{-1}$) than regions from the same tissue containing only necrotic myofibers (7.0 ± 0.6 $mm^{-1}$), and significantly higher than values from intact myofibers, whether from an adjacent region of the same sample (4.8 ± 0.3 $mm^{-1}$) or from healthy tissue of the wild-type C57 mouse (3.9 ± 0.2 $mm^{-1}$) used as a control. Our results suggest that the attenuation coefficient could be used as a quantitative means to identify necrotic lesions and assess skeletal muscle tissue in mouse models of human Duchenne muscular dystrophy.



**OCIS codes:** (110.4500) Optical coherence tomography; (170.6935) Tissue characterization; (100.2960) Image analysis; (290.1350) Backscattering.

## References and links

1. J. J. Pasquesi, S. C. Schlachter, M. D. Boppart, E. Chaney, S. J. Kaufman, and S. A. Boppart, "*In vivo* detection of exercised-induced ultrastructural changes in genetically-altered murine skeletal muscle using polarization-sensitive optical coherence tomography," Opt. Express **14**(4), 1547–1556 (2006).
2. B. R. Klyen, J. J. Armstrong, S. G. Adie, H. G. Radley, M. D. Grounds, and D. D. Sampson, "Three-dimensional optical coherence tomography of whole-muscle autografts as a precursor to morphological assessment of muscular dystrophy in mice," J. Biomed. Opt. **13**(1), 011003 (2008).
3. B. R. Klyen, T. Shavlakadze, H. G. Radley-Crabb, M. D. Grounds, and D. D. Sampson, "Identification of muscle necrosis in the *mdx* mouse model of Duchenne muscular dystrophy using three-dimensional optical coherence tomography," J. Biomed. Opt. **16**(7), 076013 (2011).
4. R. M. Lovering, S. B. Shah, S. J. P. Pratt, W. Gong, and Y. Chen, "Architecture of healthy and dystrophic muscles detected by optical coherence tomography," Muscle Nerve **47**(4), 588–590 (2013).
5. K. Bushby, R. Finkel, D. J. Birnkrant, L. E. Case, P. R. Clemens, L. Cripe, A. Kaul, K. Kinnett, C. McDonald, S. Pandya, J. Poysky, F. Shapiro, J. Tomezsko, and C. Constantin; DMD Care Considerations Working Group, "Diagnosis and management of Duchenne muscular dystrophy, Part 1: Diagnosis, and pharmacological and psychosocial management," Lancet Neurol. **9**(1), 77–93 (2010).
6. M. D. Grounds, H. G. Radley, G. S. Lynch, K. Nagaraju, and A. De Luca, "Towards developing standard operating procedures for pre-clinical testing in the *mdx* mouse model of Duchenne muscular dystrophy," Neurobiol. Dis. **31**(1), 1–19 (2008).
7. D. Huang, E. A. Swanson, C. P. Lin, J. S. Schuman, W. G. Stinson, W. Chang, M. R. Hee, T. Flotte, K. Gregory, C. A. Puliafito, and J. G. Fujimoto, "Optical coherence tomography," Science **254**(5035), 1178–1181 (1991).

#203628 - $15.00 USD Received 23 Jan 2014; revised 9 Mar 2014; accepted 11 Mar 2014; published 19 Mar 2014

8. W. Drexler and J. G. Fujimoto, *Optical Coherence Tomography: Technology and Applications*, Biological and Medical Physics, Biomedical Engineering (Springer-Verlag Berlin Heidelberg, 2008).
9. T. Shavlakadze, J. White, J. F. Y. Hoh, N. Rosenthal, and M. D. Grounds, "Targeted expression of insulin-like growth factor-I reduces early myofiber necrosis in dystrophic *mdx* mice," Mol. Ther. **10**(5), 829–843 (2004).
10. T. Shavlakadze, M. Davies, J. D. White, and M. D. Grounds, "Early regeneration of whole skeletal muscle grafts is unaffected by overexpression of IGF-1 in MLC/mIGF-1 transgenic mice," J. Histochem. Cytochem. **52**(7), 873–883 (2004).
11. M. D. Grounds, M. Davies, J. Torrisi, T. Shavlakadze, J. White, and S. Hodgetts, "Silencing TNFalpha activity by using Remicade or Enbrel blocks inflammation in whole muscle grafts: an in vivo bioassay to assess the efficacy of anti-cytokine drugs in mice," Cell Tissue Res. **320**(3), 509–515 (2005).
12. R. A. McLaughlin, L. Scolaro, P. Robbins, C. Saunders, S. L. Jacques, and D. D. Sampson, "Parametric imaging of cancer with optical coherence tomography," J. Biomed. Opt. **15**(4), 046029 (2010).
13. L. Scolaro, R. A. McLaughlin, B. R. Klyen, B. A. Wood, P. D. Robbins, C. M. Saunders, S. L. Jacques, and D. D. Sampson, "Parametric imaging of the local attenuation coefficient in human axillary lymph nodes assessed using optical coherence tomography," Biomed. Opt. Express **3**(2), 366–379 (2012).
14. P. Gong, R. A. McLaughlin, Y. M. Liew, P. R. T. Munro, F. M. Wood, and D. D. Sampson, "Assessment of human burn scars with optical coherence tomography by imaging the attenuation coefficient of tissue after vascular masking," J. Biomed. Opt. **19**(2), 021111 (2014).
15. L. Chin, X. Yang, R. A. McLaughlin, P. B. Noble, and D. D. Sampson, "*En face* parametric imaging of tissue birefringence using polarization-sensitive optical coherence tomography," J. Biomed. Opt. **18**(6), 066005 (2013).
16. X. Yang, L. Chin, B. R. Klyen, T. Shavlakadze, R. A. McLaughlin, M. D. Grounds, and D. D. Sampson, "Quantitative assessment of muscle damage in the *mdx* mouse model of Duchenne muscular dystrophy using polarization-sensitive optical coherence tomography," J. Appl. Physiol. **115**(9), 1393–1401 (2013).
17. D. Levitz, L. Thrane, M. H. Frosz, P. E. Andersen, C. B. Andersen, S. Andersson-Engels, J. Valanciunaite, J. Swartling, and P. R. Hansen, "Determination of optical scattering properties of highly-scattering media in optical coherence tomography images," Opt. Express **12**(2), 249–259 (2004).
18. F. J. van der Meer, D. J. Faber, J. Perrée, G. Pasterkamp, D. Baraznji Sassoon, and T. G. van Leeuwen, "Quantitative optical coherence tomography of arterial wall components," Lasers Med. Sci. **20**(1), 45–51 (2005).
19. C. Y. Xu, J. M. Schmitt, S. G. Carlier, and R. Virmani, "Characterization of atherosclerosis plaques by measuring both backscattering and attenuation coefficients in optical coherence tomography," J. Biomed. Opt. **13**(3), 034003 (2008).
20. G. van Soest, T. Goderie, E. Regar, S. Koljenović, G. L. J. H. van Leenders, N. Gonzalo, S. van Noorden, T. Okamura, B. E. Bouma, G. J. Tearney, J. W. Oosterhuis, P. W. Serruys, and A. F. W. van der Steen, "Atherosclerotic tissue characterization *in vivo* by optical coherence tomography attenuation imaging," J. Biomed. Opt. **15**(1), 011105 (2010).
21. Y. Yang, T. Wang, N. C. Biswal, X. Wang, M. Sanders, M. Brewer, and Q. Zhu, "Optical scattering coefficient estimated by optical coherence tomography correlates with collagen content in ovarian tissue," J. Biomed. Opt. **16**(9), 090504 (2011).
22. Y. Yang, T. Wang, X. Wang, M. Sanders, M. Brewer, and Q. Zhu, "Quantitative analysis of estimated scattering coefficient and phase retardation for ovarian tissue characterization," Biomed. Opt. Express **3**(7), 1548–1556 (2012).
23. A. M. Zysk, S. G. Adie, J. J. Armstrong, M. S. Leigh, A. Paduch, D. D. Sampson, F. T. Nguyen, and S. A. Boppart, "Needle-based refractive index measurement using low-coherence interferometry," Opt. Lett. **32**(4), 385–387 (2007).
24. H. Radley-Crabb, J. Terrill, T. Shavlakadze, J. Tonkin, P. Arthur, and M. Grounds, "A single 30 min treadmill exercise session is suitable for 'proof-of concept studies' in adult mdx mice: A comparison of the early consequences of two different treadmill protocols," Neuromuscul. Disord. **22**(2), 170–182 (2012).
25. T. G. van Leeuwen, D. J. Faber, and M. C. Aalders, "Measurement of the axial point spread function in scattering media using single-mode fiber-based optical coherence tomography," IEEE J. Sel. Top. Quantum Electron. **9**(2), 227–233 (2003).
26. W. F. Cheong, S. A. Prahl, and A. J. Welch, "A review of the optical properties of biological tissues," IEEE J. Quantum Electron. **26**(12), 2166–2185 (1990).
27. G. Hall, S. L. Jacques, K. W. Eliceiri, and P. J. Campagnola, "Goniometric measurements of thick tissue using Monte Carlo simulations to obtain the single scattering anisotropy coefficient," Biomed. Opt. Express **3**(11), 2707–2719 (2012).
28. A. N. Bashkatov, E. A. Genina, and V. V. Tuchin, "Optical properties of skin, subcutaneous, and muscle tissues: A review," J. Innov. Opt. Health Sci. **04**(01), 9–38 (2011).
29. J. J. Xia, E. P. Berg, J. W. Lee, and G. Yao, "Characterizing beef muscles with optical scattering and absorption coefficients in VIS-NIR region," Meat Sci. **75**(1), 78–83 (2007).
30. A. M. K. Nilsson, R. Berg, and S. Andersson-Engels, "Measurements of the optical properties of tissue in conjunction with photodynamic therapy," Appl. Opt. **34**(21), 4609–4619 (1995).
31. C. R. Simpson, M. Kohl, M. Essenpreis, and M. Cope, "Near-infrared optical properties of *ex vivo* human skin and subcutaneous tissues measured using the Monte Carlo inversion technique," Phys. Med. Biol. **43**(9), 2465–2478 (1998).
32. S. L. Jacques, "Optical properties of biological tissues: A review," Phys. Med. Biol. **58**(11), R37–R61 (2013).

#203628 - $15.00 USD Received 23 Jan 2014; revised 9 Mar 2014; accepted 11 Mar 2014; published 19 Mar 2014

33. R. Drezek, A. Dunn, and R. Richards-Kortum, "Light scattering from cells: Finite-difference time-domain simulations and goniometric measurements," Appl. Opt. **38**(16), 3651–3661 (1999).
34. B. C. Quirk, R. A. McLaughlin, A. Curatolo, R. W. Kirk, P. B. Noble, and D. D. Sampson, "*In situ* imaging of lung alveoli with an optical coherence tomography needle probe," J. Biomed. Opt. **16**(3), 036009 (2011).
35. D. Lorenser, X. Yang, R. W. Kirk, B. C. Quirk, R. A. McLaughlin, and D. D. Sampson, "Ultrathin side-viewing needle probe for optical coherence tomography," Opt. Lett. **36**(19), 3894–3896 (2011).
36. X. Yang, D. Lorenser, R. A. McLaughlin, R. W. Kirk, M. Edmond, M. C. Simpson, M. D. Grounds, and D. D. Sampson, "Imaging deep skeletal muscle structure using a high-sensitivity ultrathin side-viewing optical coherence tomography needle probe," Biomed. Opt. Express **5**(1), 136–148 (2014).
37. K. A. Vermeer, J. Mo, J. J. A. Weda, H. G. Lemij, and J. F. de Boer, "Depth-resolved model-based reconstruction of attenuation coefficients in optical coherence tomography," Biomed. Opt. Express **5**(1), 322–337 (2014).

## 1. Introduction

Optical coherence tomography (OCT) has shown promise for imaging skeletal muscle and identifying the morphology of healthy and pathological tissue associated with muscular dystrophy [1–4]. Duchenne muscular dystrophy (DMD) is the most severe form of this family of diseases, characterized by the progressive degeneration of skeletal and cardiac muscle tissue that eventually results in death largely from respiratory or cardiac failure [5]. Mouse models are routinely used in pre-clinical studies aimed at understanding the cause and progression of the disease, and assessing the effectiveness of potential therapies [6]. We have previously investigated OCT imaging of skeletal muscle pathology from two mouse models: the whole-muscle autograft (WMA) surgical model of muscle damage and inflammation [2]; and the X-chromosome-linked muscular dystrophy (*mdx*) mouse model of human DMD [3]. OCT is an imaging modality capable of acquiring three-dimensional (3D) scans of biological tissue with a resolution of 1 – 20 μm at depths up to 1 ~2 mm [7, 8]. Our studies have found that regions of skeletal muscle that have a different tissue composition, associated with damage and pathology, have distinct OCT signatures. Healthy skeletal muscle displays a striation pattern due to the regular arrangement of intact myofibers. In contrast, *en face* OCT images from damaged and pathological muscle tissue generally exhibit low signal and low contrast between features, leading to the greater prominence of speckle within these regions. Areas of severe pathology in the dystrophic skeletal muscles of *mdx* mice are termed necrotic lesions and typically contain necrotic myofibers with fragmented sarcolemma (cell membrane) and sarcoplasm (cellular contents), infiltrating inflammatory cells, adipose tissue, and connective tissue [9]. In the WMA surgical model of muscle damage and inflammation [10, 11], we observed a similar OCT signature in areas of the graft muscle that had undergone an inflammatory response, including that the OCT reflectance signal was attenuated at a greater rate within the damaged and inflammation regions of the graft when compared to the adjacent healthy regions of the host tissue [2], in part motivating the current study. Whilst OCT imaging has been able to show a difference between tissues of different composition, we would like to improve the extent of this differentiation and increase the contrast of tissue pathology associated with muscular dystrophy. Also, the ability to characterize a volume of tissue with an automated method is highly desirable and would enable large muscle samples to be assessed quickly. We have been developing such methods based on parametric OCT imaging of attenuation coefficients in lymph nodes [12, 13] and skin burns [14], and birefringence in tendons [15] and muscle [16]. These quantitative techniques have the advantage that they are transferrable between samples, experiments and platforms. Here, we report the use of quantitative parametric OCT imaging of the attenuation coefficient of muscle.

Previous studies have shown that the attenuation coefficient measured with OCT can be used to identify and distinguish between different types of tissue for applications such as atherosclerotic plaques in arterial segments [17–20], lymph nodes involved with human breast cancer [12, 13], and cancerous ovarian tissue [21, 22]. Whilst a number of studies have reported optical properties of skeletal muscle tissue, most of these have been measured in the

#203628 - $15.00 USD Received 23 Jan 2014; revised 9 Mar 2014; accepted 11 Mar 2014; published 19 Mar 2014

visible to near-infrared wavelength range ~400 – 1000 nm. To our knowledge, there have been no reports measuring the absolute attenuation $\mu_t$ or scattering $\mu_s$ coefficients around 1300 nm, none using OCT, and none focusing on dystrophic skeletal muscle associated with muscular dystrophy. We hypothesized that areas of skeletal muscle with different tissue composition, due to the pathology associated with muscular dystrophy, would have different optical properties.

In this paper, we report for the first time the attenuation coefficients measured with OCT at 1320 nm of skeletal mouse muscle pathology related to muscular dystrophy, from regions of tissue containing a predominance of one of four of the following: (i) & (ii) intact myofibers (either from (i) healthy control C57 mice or (ii) dystrophic *mdx* mice); (iii) necrotic myofibers (dystrophic *mdx* mice); and (iv) necrotic lesions (dystrophic *mdx* mice). Using a previously established method [13], we obtain the total attenuation coefficients on a microscopic resolution scale from 3D-OCT data sets of healthy and dystrophic muscle tissue. We show quantitative parametric maps of $\mu_t(x,y)$ that display better contrast and improve on OCT imaging for the identification of regions of pathology, namely necrotic lesions surrounded by intact myofibers, within the skeletal muscles of dystrophic *mdx* mice. We report the range of attenuation coefficients measured by OCT from specific tissue compositions, which were subsequently confirmed by correlation with co-located histology. Our results demonstrate the ability of 3D-OCT to measure the attenuation coefficient of skeletal muscle tissue and generate parametric maps that improve the identification and contrast of pathology associated with muscular dystrophy. Such methods could contribute towards improving pre-clinical studies of therapies for DMD.

## 2. Materials and methods

### *2.1 Optical coherence tomography imaging*

The system and experimental protocol used to obtain 3D-OCT scans for generating images [3] and extracting the attenuation coefficients [13] has been previously described. Briefly, the custom-built time-domain OCT system (TD-OCT) uses a 14 mW light source operating at a center wavelength of 1320 nm with a 3 dB bandwidth of 154 nm, to give a measured axial resolution of ~8 µm in air. Axial scanning was achieved using a frequency-domain optical delay line (FD-ODL) in the reference arm, operating at 500 Hz over a range of 2.2 mm in air. The imaging beam illuminated the sample via an objective lens with a numerical aperture of 0.07, giving a measured lateral resolution of ~11µm in air. 3D scan volumes measuring 3 × 6 × 2.2 mm (*x*, *y*, *z*) were obtained by lateral scanning of the beam via a galvanometer mirror (*x*-axis) and linear translation of the sample (*y*-axis). The resulting backscattered interference signal was detected using a dual-balanced photodetector, and bandpass filtered and logarithmically demodulated in hardware for envelope detection, before analog-to-digital conversion and data acquisition on a grid with spacings 3.4 µm × 5.9 µm × 2.1 µm (*x*, *y*, *z*). The measured sensitivity of the system was ~105 dB.

*Ex vivo* skeletal muscle samples were imaged from below through a glass window whilst immersed in phosphate buffered saline (PBS) ($n_{PBS}$ = 1.32), which prevented dehydration and achieved index matching between the glass and tissue. Samples were positioned such that the majority of the muscle's myofibers were aligned orthogonal to the optical axis and parallel to the *en face* (*x*-*y*) OCT image plane. The focus of the imaging beam was positioned 500 µm (in air) beyond the glass/air interface, equivalent to ~700 µm into the tissue, assuming a refractive index of $n_{tissue}$ ~1.4 [23].

The logarithmically demodulated OCT signal was displayed on a gray scale in which white represents the highest signal, and the contrast was adjusted to best identify the anatomical features of interest. Multiplanar reformatting was applied to the 3D-OCT scans using custom software to manually extract *en face* images (3 × 6 mm). Structural features of

#203628 - $15.00 USD Received 23 Jan 2014; revised 9 Mar 2014; accepted 11 Mar 2014; published 19 Mar 2014

interest were used to optimally match, by inspection, the *en face* (*x*-*y*) OCT images to the histological sections at the same depth.

### *2.2 Mouse model, sampling and histology*

Five *mdx* (C57Bl/10ScSn$^{mdx/mdx}$) and three wild-type C57 (C57Bl/10ScSn), male nine-week-old mice were obtained from the Animal Resources Centre, Murdoch, Western Australia. All animal experiments were conducted in strict accordance with the guidelines of the National Health & Medical Research Council Code of Practice for the Care and Use of Animals for Scientific Purposes (2004) and the Animal Welfare Act of Western Australia (2002) and were approved by the Animal Ethics Committee of The University of Western Australia.

All five *mdx* mice completed a horizontal treadmill running protocol at 12 m/min for 30 min, which increases *mdx* myofiber damage so that ~10 – 15% of the total cross-sectional area of the muscle contains necrotic myofibers [24]. It is noted that areas of active recent necrosis (induced by exercise) occur in addition to the background pathology of muscles with ongoing endogenous cycles of focal necrosis and regeneration. Such mild exercise does not damage the normal myofibers of C57 mice and they were not subjected to treadmill running prior to sampling. Immediately following exercise, *mdx* mice received an intraperitoneal injection of sterile 1% Evans blue dye (EBD) (w/v) in PBS. Injection of EBD is a proven method for identifying myofibers with permeable (leaky or necrotic) membranes and identifying regions of muscle damage onset [6]. We have previously established EBD as a suitable *in vivo* marker for targeted 3D-OCT imaging of muscle with leaky or necrotic myofibers [3]. The EBD-positive degenerating myofibers can be macroscopically identified by their dark blue staining, and EBD does not change the local optical properties of the tissue or act as a contrast agent at 1320 nm [3]. *Mdx* mice were sampled twenty-four hours following EBD injection, whilst C57 mice were not injected with EBD and instead just killed and sampled. All mice (both *mdx* and C57) were anaesthetized with 2% v/v Isoflurane (Bomac, Australia), $N_2O$ and $O_2$, and killed via cervical dislocation. Skeletal muscles from the hindlimb (tibialis anterior, gastrocnemus, quadriceps, gluteus) and forelimb (triceps) were removed and placed in PBS on ice for transportation and subsequent *ex vivo* 3D-OCT imaging. A total of 13 muscle samples from 8 mice (five *mdx* and three C57) were used in this study.

Following 3D-OCT imaging, samples were frozen in isopentane (cooled in liquid nitrogen) for histological sectioning. Longitudinal serial sections (8 µm thick) were cut that were closely aligned parallel to the *en face* (*x*-*y*) plane of the 3D-OCT scans, and mounted on glass slides. Sections were stained with hematoxylin and eosin (H&E) for light microscopy and digital imaging (ScanScope XT, Aperio Technologies Inc., Vista, California).

### *2.3 Extracting the attenuation coefficient*

The details of the method for extracting the attenuation coefficient from biological tissue have been reported in a previous paper [13]. Here, we summarize the main points and highlight the differences compared with the previous method.

The square of the detected OCT photocurrent $i^2(z)$ is linearly proportional to the returning power fraction, or reflectance $R_s(z)$, of light from a tissue sample at depth $z$. In turn, the reflectance for a homogenous tissue can be modeled as a decaying exponential with depth, as described by the Beer-Lambert law, on the assumption that single scattering is the dominant scattering process [25]. Additionally, the reflectance is modulated by the confocal function of the focusing optics in the sample arm, $F(z)$, and by coupling losses due to scanning of the FD-ODL in the reference arm, $S(z)$. For a homogeneous, single-scattering sample, the OCT A-scan signal power as a function of depth can, therefore, be expressed as:

$$i^2(z) \propto F(z)S(z)\rho e^{-2\mu_t z}, \tag{1}$$

#203628 - $15.00 USD Received 23 Jan 2014; revised 9 Mar 2014; accepted 11 Mar 2014; published 19 Mar 2014

where $\rho e^{-2\mu_t z}$ represents the singly scattered component, $\rho$ is the initial value of reflectance, $\mu_t$ [mm$^{-1}$] is the attenuation coefficient, and the factor of 2 in the exponent accounts for the double pass of light propagation in the tissue.

To extract the attenuation coefficient, we first corrected our *ex vivo* 3D scans for the confocal function $F(z)$ and scanning losses $S(z)$ in our TD-OCT system. To do this, we used a calibration scan $R_0(z)$ of a diffuse-scattering, homogeneous suspension of polystyrene microspheres in water, with known reference attenuation coefficient $\mu_{t0}$, calculated using Mie theory as previously described [13]. The OCT signal power was corrected by dividing by the corresponding calibration scan for each voxel in the OCT volume. The attenuation coefficient of the tissue $\mu_t$ [mm$^{-1}$] at each lateral location ($x$-$y$) is determined by taking the natural logarithm of the corrected reflectance profile $\ln\left[R_s(z)/R_0(z)\right]$. Whilst the surface reflectivity of the sample will vary, at each lateral location ($x$, $y$) the resulting term $\ln\left[\rho_s(x,y)/\rho_0(x,y)\right]$ is a constant and can be omitted for simplicity. The resulting relationship between the corrected sample reflectance profile $\ln\left[i_s^{\,2}(z)/i_0^{\,2}(z)\right]$ and depth $z$ is linear, and directly proportional to the sample attenuation coefficient $\mu_t$ and known reference attenuation coefficient $\mu_{t0}$ as below:

$$\ln\left[\frac{i_s^{\,2}(z)}{i_0^{\,2}(z)}\right] \propto -2(\mu_t - \mu_{t0}). \tag{2}$$

For each data set, speckle noise and micro-scale tissue inhomogeneities were reduced using a moving window averaging function with a uniform kernel of 100 × 100 µm within the ($x$-$y$) plane. The attenuation coefficient $\mu_t$ was calculated using a linear least-squares fit to the averaged OCT signal power over a specified axial range. The $z$-axis was scaled to correct for the difference between physical and optical path length, taking the group refractive index of skeletal muscle to be $n_{muscle}$ = 1.4 [23]. The processing parameters that gave the most consistent results for matching the corresponding *en face* OCT images and H&E-stained histological sections across all samples were empirically determined to be an axial range of 500 µm, beginning at 100 µm beyond the glass-window / tissue interface and extending into the sample to a depth of 600 µm. *En face* parametric maps of $\mu_t(x,y)$ were generated for the axial range of $z$ = [100 µm, 600 µm], with attenuation coefficients assigned to a color map ranging $\mu_t$ = [0 mm$^{-1}$, 15 mm$^{-1}$] and negative values ($\mu_t < 0$) masked white. Corresponding *en face* ($x$-$y$) OCT images were generated at the mid-point of the processing range $z$ = 350 µm for structural comparison. H&E-stained histological sections, co-located and matched for depth with the *en face* ($x$-$y$) OCT images, are presented for all examples to identify the muscle morphology and features of interest in order to inform the parametric imaging.

Attenuation coefficients $\mu_t$ were calculated from 3D-OCT data sets obtained from selected regions of the tissue samples from all 13 muscles acquired from 8 mice. Parametric maps of $\mu_t$ for each lateral position were generated and the results qualitatively compared with co-located images of *en face* ($x$-$y$) OCT, H&E-stained histological sections and photographs of the sample. Quantitative comparisons are also made based on the distribution of $\mu_t$ displayed in a histogram from selected regions-of-interest (ROIs).

## 3. Results

We first present results from separate samples of healthy and dystrophic skeletal muscle tissue, and then compare the results from each. Next, we compare the results obtained from two ROIs selected from within the same dystrophic muscle tissue sample, and show examples of this comparison from two mice. Finally, we summarize the results of the attenuation coefficients acquired from all samples, to demonstrate that $\mu_t(x,y)$ can be used as a parameter to distinguish between skeletal muscle tissues of different composition.

#203628 - $15.00 USD Received 23 Jan 2014; revised 9 Mar 2014; accepted 11 Mar 2014; published 19 Mar 2014

*3.1 Attenuation coefficients of healthy and dystrophic skeletal muscle tissue*

We first show the results of healthy tissue in Fig. 1, obtained from the tibialis anterior skeletal muscle from the hindlimb of a wild-type C57 mouse. The parametric map $\mu_t(x,y)$ indicates that the majority of the muscle has low values of the attenuation coefficient ranging from ~2 – 6 $mm^{-1}$ [Fig. 1(d)]. These regions correspond to areas of intact myofibers in the H&E-stained section [Fig. 1(b)], which are clearly visible as elongated cells with their eosinophilic sarcoplasm stained pink, peripherally surrounded by nuclei stained dark purple by haematoxylin. Most myofibers are aligned parallel to the sectioning plane and appear as cylindrical cells cut longitudinally. In the matched *en face* OCT image [Fig. 1(c)], the corresponding regions display long hyper-scattering lines, forming the characteristic striation pattern indicative of intact myofibers in skeletal muscle tissue. These features are well aligned parallel to the plane shown, and their orientation matches the direction of myofibers seen in the H&E-stained section.

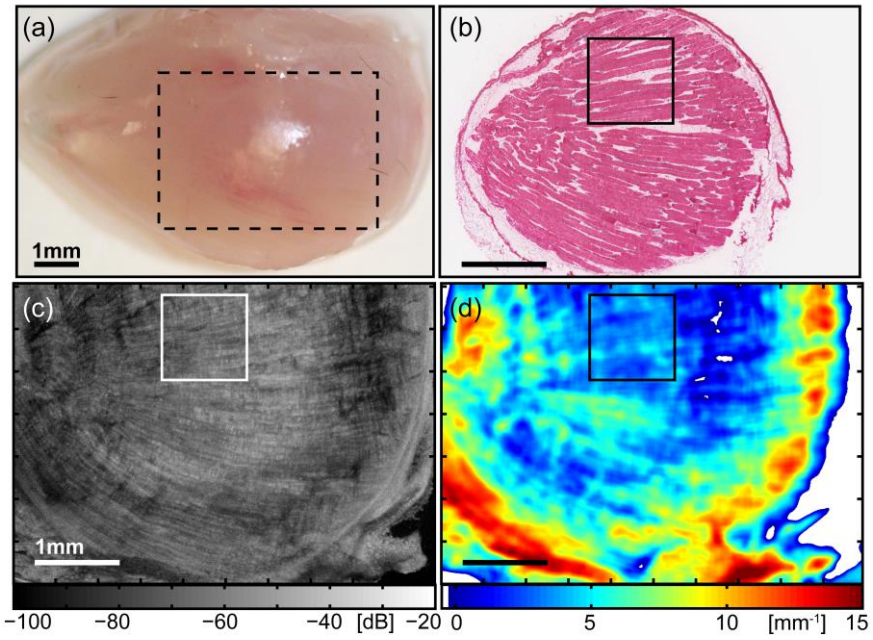


Fig. 1. Images of healthy skeletal muscle tissue, obtained from the tibialis anterior of a wild-type C57Bl/10ScSn mouse. (a) Photograph of the anterior surface of the muscle, indicating the lateral area (*x*-*y*) over which the subsequent 3D-OCT data set was obtained (dashed outline). For clarity, this image is scaled × 2 compared to the following images (b) – (d). (b) Co-registered H&E-stained histology identifying tissue morphology. (c) *En face* (*x*-*y*) OCT image at depth $z$ = 350 µm from the imaging glass-window / tissue interface. (d) Parametric map of attenuation coefficients $\mu_t(x,y)$. Points with $\mu_t < 0$ are masked white. The outlined region in images (b) – (d) indicates the ROI selected for subsequent comparison and quantitative analysis. All scale bars 1 mm.

Two image artifacts, present in this example and in subsequent results, were identified. These were high values of $\mu_t$ at the edge of the sample (here in the range ~8 – 14 $mm^{-1}$), and negative values of $\mu_t$, whether at the edge or within the sample. These artifacts are associated with areas of the muscle sample that are not in direct contact with the glass-window, or with the presence of a layered structure (*i.e.*, not homogeneous) in the sample. Based on this initial analysis, only lateral regions (*x*-*y*) of the sample (identified in the 3D-OCT data set) that (i) contain one tissue type over the fitting range, and (ii) were in direct contact with the imaging glass-window, had their calculated attenuation coefficients quantitatively compared with other regions. A region-of-interest (ROI) was selected for further examination and

#203628 - $15.00 USD Received 23 Jan 2014; revised 9 Mar 2014; accepted 11 Mar 2014; published 19 Mar 2014

quantitative comparison, subsequently seen in Fig. 3, and indicated in Fig. 1(b)-1(d) by the smaller square (1 × 1 mm). We have found that regions of intact myofibers from the muscle of normal mouse have relatively low attenuation coefficients in the range of $\mu_t$ ~2 – 6 mm$^{-1}$, and these areas displayed the characteristic OCT striation pattern of intact myofibers, as seen in our previous study. We next perform this analysis on dystrophic skeletal muscle tissue from the *mdx* mouse model of human DMD, in particular, examining the necrotic lesions associated with exercise-induced pathology.

Figure 2 shows results for a dystrophic skeletal muscle containing a necrotic lesion, obtained from the triceps of a treadmill-exercised *mdx* mouse that had been injected with EBD post-exercise. The photograph [Fig. 2(a)] shows the dorsal surface of the muscle, with the large region of blue-staining indicating an accumulation of EBD within leaky myofibers. The presence of permeable myofibers gives strong support to the supposition of muscle damage and necrosis at this location, and we used the presence of accumulated EBD to guide the subsequent 3D-OCT imaging [Fig. 2(c)].

The parametric map for the dystrophic tissue contains attenuation coefficients of relatively higher values ~9 – 12 mm$^{-1}$ for much of the area [Fig. 2(d)]. In the corresponding areas of the histology [Fig. 2(b)], the tissue is observed to be no longer well organized into rows of elongated myofibers, but is damaged and displays a disordered ultrastructure. The majority of myofibers have become necrotic and are no longer intact, with fragmented sarcolemma and spilled sarcoplasm. The density of dark purple-staining nuclei is greater in the dystrophic skeletal muscle, due to the presence of many mononucleated cells. These are infiltrating inflammatory cells, recruited in an inflammatory response to phagocytoze the necrotic myofibers. In the matching areas of the *en face* (*x*-*y*) OCT image [Fig. 2(c)], we see a lower OCT signal and loss of the striation pattern.

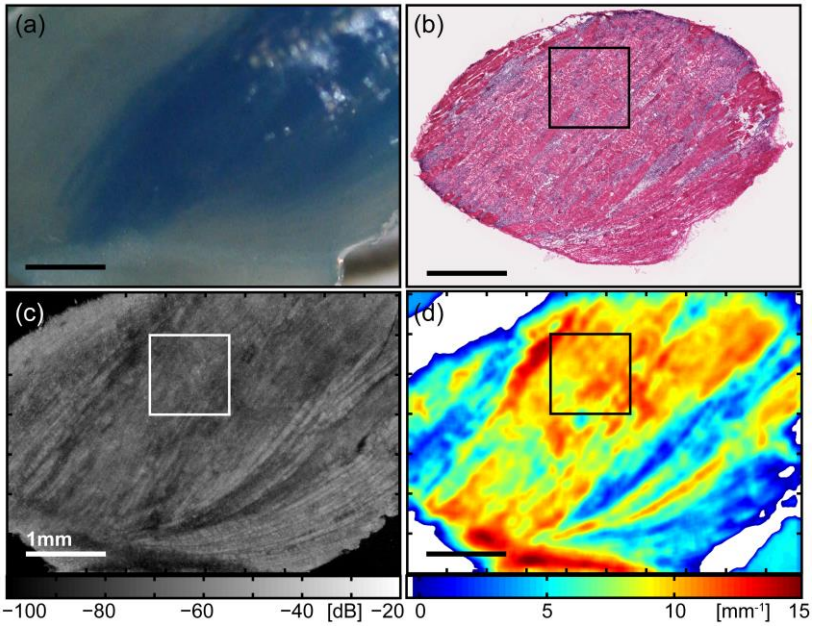


Fig. 2. Images of dystrophic skeletal muscle tissue containing a necrotic lesion, obtained from the triceps of a treadmill-exercised *mdx* mouse. (a) Photograph of the dorsal surface of the muscle showing a blue-stained region of EBD accumulation, indicating the presence of leaky myofibers. (b) Co-registered H&E-stained histology identifying tissue morphology. (c) *En face* (*x*-*y*) OCT image at depth z = 350 µm from the imaging glass-window / tissue interface. (d) Parametric map of attenuation coefficients $\mu_t(x,y)$. Points with $\mu_t < 0$ are masked white. The outlined region in (b) – (d) indicates the ROI selected for subsequent comparison and quantitative analysis. All scale bars 1 mm.

#203628 - $15.00 USD Received 23 Jan 2014; revised 9 Mar 2014; accepted 11 Mar 2014; published 19 Mar 2014

Conversely, two prominent areas have lower attenuation coefficients. These match the hyper-scattering striation regions seen at the bottom right of the OCT image, indicating intact myofibers, as confirmed by the corresponding H&E-stained section. Here, the intact (non-necrotic) myofibers remaining in this sample can be seen as two strips of pink-staining areas located in the lower right of the section, separated by an area of densely populated, dark purple-staining nuclei of infiltrating inflammatory cells. The range of lower values of attenuation coefficients ~3 – 6 $mm^{-1}$ extracted from this area of intact myofibers of dystrophic muscle from the *mdx* mouse are similar to those results obtained from intact myofibers of the healthy muscle from the C57 mouse, shown in Fig. 1. The feature in the bottom left corner of the parametric map with high attenuation coefficient ~13 – 15 $mm^{-1}$ is the connective tissue between the different heads of the triceps brachii muscle (long, lateral, medial), visible as a white structure running horizontally along the bottom of the photograph [Fig. 2(a)]. The high $\mu_t$ value here is due to the sharp drop-off in the reflectance profile caused by the shadowing effect of this high-scattering feature, as seen in the *en face* OCT image [Fig. 2(c)]. The parametric map of attenuation coefficients improves the contrast between the two main areas of dystrophic skeletal muscle tissue with different compositions: regions of intact myofibers or necrotic lesions containing necrotic myofibers and inflammatory cells. These two tissue compositions are further analyzed and their attenuation coefficients quantitatively compared in the following section.

The two samples with different tissue compositions are compared in Fig. 3: qualitatively, using the zoomed parametric maps of attenuation coefficients $\mu_t(x,y)$ and images obtained from *en face* OCT, supported by the corresponding H&E-stained histology; and quantitatively, based on the distribution of $\mu_t(x,y)$. The parametric maps of $\mu_t(x,y)$ [Fig. 3(c) and 3(f)] show strong contrast between the tissue types. The intact myofibers from healthy muscle display lower values in the range ~2 – 5 $mm^{-1}$, whilst the necrotic lesion from the dystrophic muscle displays values predominantly in the range ~8 – 12 $mm^{-1}$. The *en face* OCT images [Fig. 3(b) and 3(e)] display limited contrast between them. Figure 3(b) shows the characteristic high-signal OCT striations, which are well aligned with the structurally intact individual myofibers (IM, white arrowheads) that are surrounded by dark purple-staining nuclei on their periphery (PN, thin white arrows) as shown in the corresponding H&E-stained section [Fig. 3(a)]. The OCT image [Fig. 3(e)] obtained from within a necrotic lesion of dystrophic muscle lacks this striation pattern and instead is featureless with prominent speckle. The corresponding histology [Fig. 3(d)] shows a distinctly different tissue composition that is composed mainly of necrotic myofibers (NM, black arrowheads) with fragmented sarcoplasm, densely surrounded by mononucleated inflammatory cells (IC, thick black arrows) with their dark purple-staining nuclei. To summarize, at this scale, the contrast between the two *en face* OCT images is low, whereas, that of the parametric images of $\mu_t(x,y)$ is much higher.

The two regions are quantitatively compared in the histogram [Fig. 3(g)] that presents the distribution of attenuation coefficients for the selected 1 × 1 $mm^2$ ROIs from the two different tissue compositions. Each histogram contains typically ~46,000 values, corresponding to the number of reflectance profiles in the A-scans from each ROI, that have been grouped in bins of width $\Delta\mu_t$ = 0.5 $mm^{-1}$, normalized and their respective frequencies plotted as a bar chart. The ROI containing intact myofibers from healthy tissue, corresponding to the top row (a) – (c) (green outline), has a histogram (green) closely approximating the fitted normal distribution (dashed line) with values ranging from 1.5 – 5.5 $mm^{-1}$, giving $\mu_t$ = 3.4 ± 0.7 $mm^{-1}$ (mean ± standard deviation). The ROI from within a necrotic lesion from dystrophic muscle tissue, corresponding to the middle row (d) – (f) (red outline), has a histogram (red) closely approximating the fitted normal distribution (dot-dashed line), but with a wider spread of values ranging from 6.5 – 13.5 $mm^{-1}$, giving $\mu_t$ = 10.0 ± 1.0 $mm^{-1}$ (mean ± standard deviation).

#203628 - $15.00 USD Received 23 Jan 2014; revised 9 Mar 2014; accepted 11 Mar 2014; published 19 Mar 2014

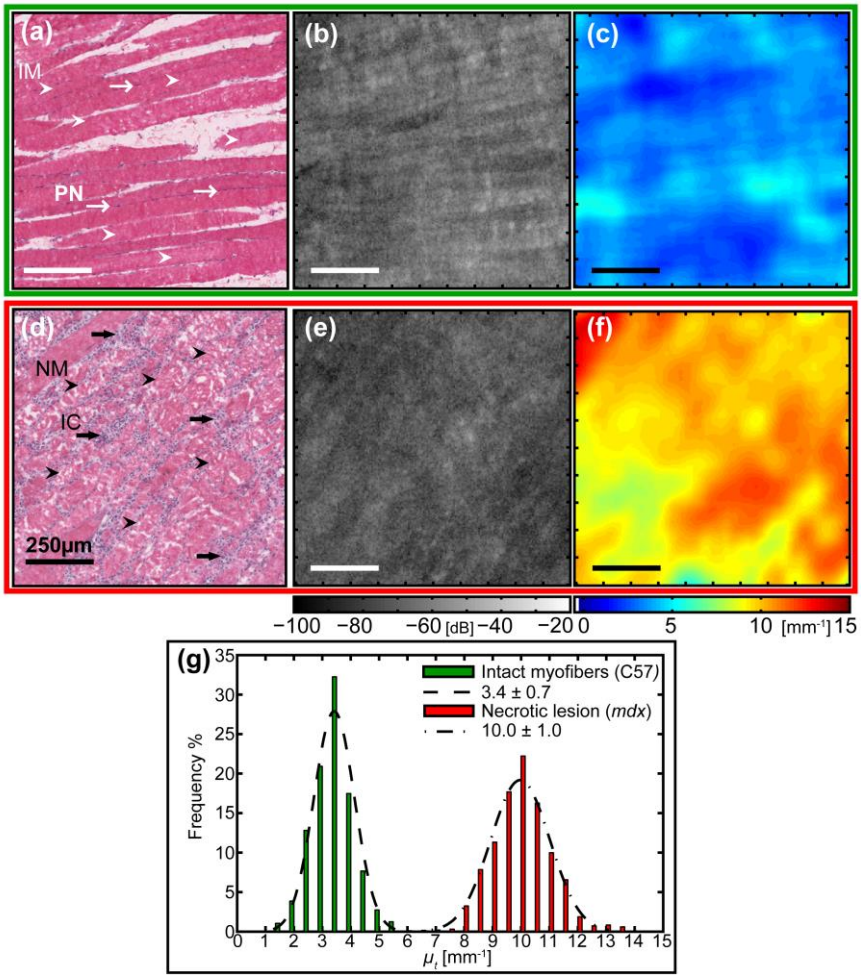


Fig. 3. Quantitative comparison of the attenuation coefficients obtained from a region of intact myofibers within healthy skeletal muscle tissue and a necrotic lesion from within dystrophic skeletal muscle tissue. (a) – (c) Top Row (green outline): Intact myofibers of the tibialis anterior skeletal muscle from a healthy C57 mouse. (d) – (f) Bottom row (red outline): Necrotic lesion containing necrotic myofibers and inflammatory cells, from the triceps skeletal muscle of a treadmill-exercised dystrophic *mdx* mouse. (a) & (d) Co-registered H&E-stained histology indicating biological features of interest: (a) intact myofibers (IM, white arrowheads), peripheral nuclei (PN, thin white arrows); (d) necrotic myofibers (NM, black arrowheads), inflammatory cells (IC, thick black arrows). (b) & (e) Zoomed *en face* (*x*, *y*) OCT image at depth $z$ = 350 μm from the imaging glass-window / tissue interface. (f) & (g) Parametric maps of attenuation coefficients $\mu_t(x,y)$. All scale bars 250 μm. (g) Histogram of attenuation coefficients $\mu_t$ for the selected ROIs containing intact myofibers from healthy tissue (green) and a necrotic lesion from dystrophic skeletal muscle tissue (red), with associated normal distribution (dashed and dot-dashed, respectively) fitted using the calculated mean ± standard deviation.

### *3.2 Comparison of different tissues within a dystrophic sample*

The two different tissue compositions analyzed above, intact myofibers and a necrotic lesion obtained from different mice, have distinctly different attenuation coefficients. We now apply the same analysis technique to measure this optical property in regions of different tissue composition within the same pathological muscle sample, presented in two examples. This is to determine whether $\mu_t(x,y)$ is a suitable parameter for identifying necrotic lesions and

#203628 - $15.00 USD Received 23 Jan 2014; revised 9 Mar 2014; accepted 11 Mar 2014; published 19 Mar 2014

improving the contrast between different tissue compositions associated with pathology in the skeletal muscle tissue of dystrophic treadmill-exercised *mdx* mice. In this first example, we investigate and compare two ROIs from within the dystrophic triceps skeletal muscle of a treadmill-exercised *mdx* mouse: one containing mainly intact myofibers, and another from within a necrotic lesion.

The parametric maps of attenuation coefficients show a high degree of contrast between tissues of different composition. The whole sample [Fig. 4(c)] displays a background of low values ~1 – 6 $mm^{-1}$ strongly contrasted with two areas (black dashed outline) of relatively higher values ~8 – 12 $mm^{-1}$. The areas of low $\mu_t$ (black @, Fig. 4(c)) match well with zones containing predominantly intact myofibers in the H&E-stained section (white asterisks, Fig. 4(a)) and striation patterns (white @s, Fig. 4(b)) in the OCT image. The larger, horizontal strip of high $\mu_t$ (black hashtag, Fig. 4(c)) matches well with a large necrotic lesion identified in the corresponding H&E-section (black asterisk, Fig. 4(a)) and the disruption region in the *en face* OCT image (white hashtag, Fig. 4(b)). A smaller area of high $\mu_t$ (black hashtag, Fig. 4(c)) also matches a corresponding necrotic lesion (black asterisk, Fig. 4(a)) and disruption region (white hashtag, Fig. 4(b)), although to a lesser degree. Whilst it is difficult to see the necrotic lesions based on their subtle OCT signature in the *en face* OCT images alone, their identification is strongly improved by qualitative inspection of the associated parametric map of attenuation coefficients.

The zoomed images [Fig. 4(d)-4(i)] further highlight the improvement in contrast offered by parametric maps of the attenuation coefficient $\mu_t(x,y)$. Two ROIs of different tissue composition from within the same sample are chosen and compared (both 1 $mm^2$ and matched in dimensions). The first ROI (blue outline) is composed mainly of intact myofibers (IM, white arrowheads) with centrally located nuclei (CN, thin black arrows), which indicates they have undergone at least one cycle of necrosis and regeneration. Also present are mononucleated inflammatory cells (IC, thick black arrows) [Fig. 4(d)]. The second ROI (red outline) is within the larger necrotic lesion and is comprised primarily of disordered necrotic myofibers (NM, black arrowheads) with disintegrating sarcoplasm, surrounded by mononucleated inflammatory cells (thick black arrows) [Fig. 4(g)]. Here, the nuclei density is higher compared with the ROI containing mainly intact myofibers. Also visible are some regenerated intact myofibers (white arrowheads) readily identified by their centrally located nuclei (thin black arrow); and white, small globular appearing cells with no cytoplasmic staining, presumably adipocytes (AC, double-headed white arrow). Whilst the necrotic lesions can be identified by interactively viewing the 3D-OCT volumetric data set, the contrast between regions of intact myofibers and necrotic lesions is relatively low, as seen in the matching zoomed *en face* OCT images [Fig. 4(e) and 4(h), respectively]. The co-located parametric maps of $\mu_t(x,y)$ [Fig. 4(f) and 4(i)] show a high level of contrast between the two ROIs of differing tissue composition, and improves the ability to identify necrotic lesions from surrounding intact myofibers.

The two ROIs are quantitatively compared in a histogram [Fig. 4(j)]. The region of intact myofibers, corresponding to the middle row (d) – (f) (blue outline), has a histogram (blue) closely approximating the fitted normal distribution (dashed line) with values ranging 0.5 – 7.0 $mm^{-1}$, giving $\mu_t$ = 3.7 ± 1.1 $mm^{-1}$ (mean ± standard deviation). This is well separated from the ROI obtained from within the necrotic lesion, corresponding to the bottom row (g) – (i) (red outline), which has a histogram (red) reasonably approximating the fitted normal distribution (dot-dashed line) with values ranging 8.0 – 11.5 $mm^{-1}$, giving $\mu_t$ = 10.1 ± 0.7 $mm^{-1}$ (mean ± standard deviation). The two distributions are well separated on the histogram. The two different tissue compositions can be distinguished based on the calculated attenuation coefficient values, as shown in the histogram [Fig. 4(g)] and also based on the large contrast between the corresponding parametric maps of $\mu_t(x,y)$ [Fig. 4(f) and 4(i)].

#203628 - $15.00 USD Received 23 Jan 2014; revised 9 Mar 2014; accepted 11 Mar 2014; published 19 Mar 2014

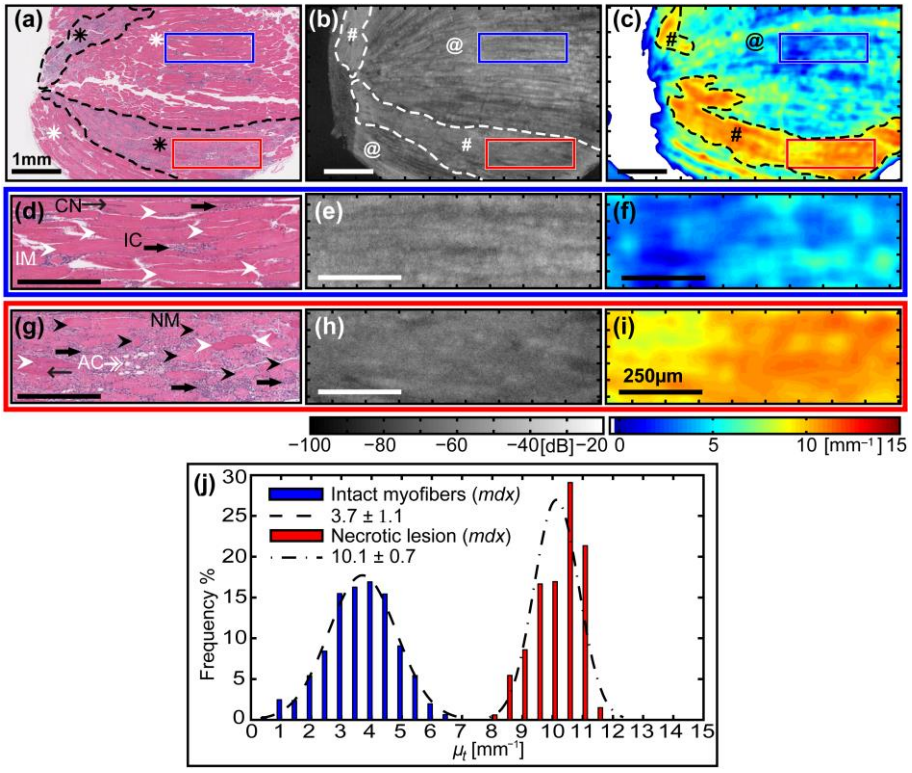


Fig. 4. Quantitative comparison of the attenuation coefficients obtained from two different regions, intact myofibers and a necrotic lesion, selected from within the same sample of dystrophic skeletal muscle tissue. (a) – (c) Top row: Images of the entire muscle sample (symbols described in the text). Scale bars 1 mm. (d) – (f) Middle row (blue outline): Zoomed images from the region of intact myofibers. Scale bars 250 μm. (g) – (i) Bottom row (red outline): Zoomed images from the necrotic lesion containing necrotic myofibers and inflammatory cells. (a), (d) & (g) Co-registered H&E-stained histology indicating biological features of interest: (d) intact myofibers (IM, white arrowheads), central nuclei (CN, thin black arrows), and inflammatory cells (IC, thick black arrows); (g) necrotic myofibers (NM, black arrowheads) and adipose cells (AC, doubled-headed white arrow). (b), (e) & (h) *En face* (*x*-*y*) OCT images at depth $z$ = 350 μm from imaging glass-window / tissue interface. (c), (f) & (i) Parametric maps of attenuation coefficients $\mu_t(x,y)$. Points with $\mu_t < 0$ are masked white. (j) Histogram of attenuation coefficients $\mu_t$ for intact myofibers (blue) versus a necrotic lesion (red) from within the dystrophic skeletal muscle tissue, with an associated normal distribution fitted using the mean ± standard deviation calculated from each chosen ROI.

In the next example [Fig. 5], we present an additional different tissue composition found within the gluteus skeletal muscle of a treadmill-exercised dystrophic *mdx* mouse. The parametric map of $\mu_t(x,y)$ [Fig. 5(c)] shows contrast between the two halves of the sample (separated by black dashed line). The left side has a range of higher values of $\mu_t$ ~5 – 8 mm$^{-1}$ (black ampersand) that matches well with the different tissue composition containing necrotic myofibers without inflammatory cells identified in the corresponding H&E-section (black hashtag, Fig. 5(a)). The right side has a range of lower values of $\mu_t$ ~2 – 6 mm$^{-1}$ (white @s, Fig. 5(c)) that matches with an area containing predominantly intact myofibers (white asterisks, Fig. 5(a)). Also seen within this half is a sub-region (dot-dashed line) of slightly higher $\mu_t$ values (black @, Fig. 5(c)) that is co-located with a vertically aligned necrotic lesion (black asterisk, Fig. 5(a)). This distinction is not readily apparent in the co-located *en face* OCT [Fig. 5(b)], and mapping the attenuation coefficients has improved our ability to differentiate between the three different tissue compositions present in this one sample.

#203628 - $15.00 USD Received 23 Jan 2014; revised 9 Mar 2014; accepted 11 Mar 2014; published 19 Mar 2014

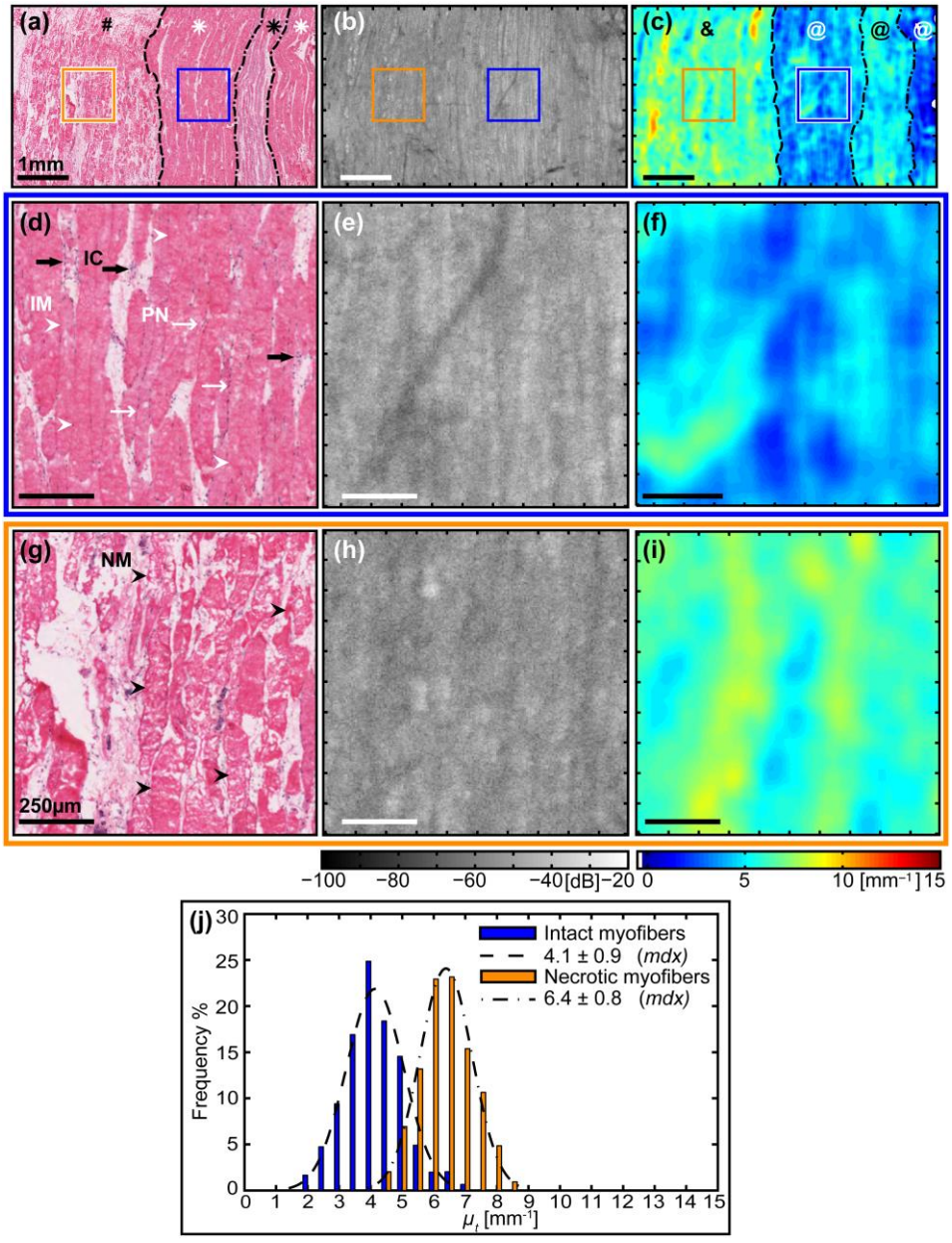


Fig. 5. Quantitative comparison of the attenuation coefficients from two different regions, intact myofibers versus necrotic myofibers without inflammatory cells, from within the same sample of dystrophic skeletal muscle tissue. (a) – (c) Top row: Large-scale images of the muscle sample (symbols described in the text). Scale bars 1 mm. (d) – (f) Middle row (blue outline): Zoomed images of intact myofibers. Scale bars 250 μm. (g) – (i) Bottom row (orange outline): Zoomed images of necrotic myofibers without the presence of inflammatory cells. Scale bars 250 μm. (a), (d) & (g) Co-registered H&E-stained histology indicating biological features of interest: (d) intact myofibers (IM, white arrowheads), peripheral nuclei (PN, thin white arrows), and inflammatory cells (IC, thick black arrows); (g) necrotic myofibers (NM, black arrowheads). (b), (e) & (h) *En face* (*x*-*y*) OCT images. (c), (f) & (i) Parametric maps of attenuation coefficients $\mu_t(x, y)$. (j) Histogram of attenuation coefficients $\mu_t$ for intact myofibers (blue) versus necrotic myofibers (without inflammatory cells) with an associated normal distribution fitted using the mean ± standard deviation calculated from each ROI.

#203628 - $15.00 USD Received 23 Jan 2014; revised 9 Mar 2014; accepted 11 Mar 2014; published 19 Mar 2014

The zoomed images [Fig. 5(d)-5(i)] highlight the improved contrast using the calculated parametric maps of $\mu_t(x,y)$ to differentiate between the two distinct tissue compositions in two ROIs. The first ROI (blue outline) is comprised predominantly of intact myofibers (IM, white arrowheads) with nuclei located at the periphery (PN, thin white arrows), which indicates they are surviving myofibers [Fig. 5(d)]. Also present are small pockets (~50 μm length) of mononucleated inflammatory cells (IC, thick black arrows). The second ROI (orange outline) has a different composition: predominantly necrotic myofibers (NM, black arrowheads) with fragmented sarcoplasm, but without a noticeable presence of inflammatory cells [Fig. 5(g)]. The zoomed *en face* OCT images [Fig. 5(e) and 5(h)] corresponding to intact and necrotic myofibers, respectively, are similar in appearance with an overall comparable signal level and relatively low contrast between them. The co-located parametric maps $\mu_t(x,y)$ [Fig. 5(f) and 5(i)] show a much higher degree of contrast between the two regions of differing tissue composition.

The two ROIs are quantitatively compared in the histogram [Fig. 5(j)]. The region of intact myofibers, corresponding to the middle row (d) – (f) (blue outline), has a histogram (blue) closely approximating the fitted normal distribution (dashed line) with values ranging 2.0 – 7.0 $mm^{-1}$, giving $\mu_t = 4.1 \pm 0.9$ $mm^{-1}$ (mean ± standard deviation). This distribution is offset from that obtained from the ROI containing necrotic myofibers without inflammatory cells, corresponding to the bottom row (g) – (i) (orange outline), which has a histogram (orange) closely approximating the fitted normal distribution (dot-dashed line) with values spanning a slightly higher range 4.5 – 8.5 $mm^{-1}$, giving $\mu_t = 6.4 \pm 0.8$ $mm^{-1}$ (mean ± standard deviation). Whilst there is a degree of overlap between the values of $\mu_t$ for each ROI, the two distributions are separated by ~2.5 $mm^{-1}$, which is sufficient to distinguish the different tissue compositions based on the attenuation coefficient.

### *3.3 Overall assessment of attenuation coefficient*

A total of 28 non-overlapping 1 $mm^2$ ROIs from 13 muscles obtained from 8 mice were imaged and analyzed for the attenuation coefficient. The attenuation coefficient (mean ± standard error) of skeletal muscle tissue in regions containing intact myofibers from C57 mice muscles (n = 10), intact myofibers from *mdx* mice muscles (n = 10), necrotic myofibers from *mdx* mice muscles (n = 2), and necrotic lesions from *mdx* mice muscles (n = 6), was calculated from data from all available muscle samples [Fig. 6]. Generally, regions containing intact myofibers have the lowest attenuation coefficient, whether from healthy C57 mice (3.9 ± 0.2 $mm^{-1}$) or dystrophic *mdx* mice (4.8 ± 0.3 $mm^{-1}$). Necrotic lesions give rise to the highest attenuation coefficient (9.6 ± 0.3 $mm^{-1}$). Interestingly, areas containing necrotic myofibers with their fragmented membranes and spilled sarcoplasm, but lacking a high density of inflammatory cells, have an intermediate value (7.0 ± 0.6 $mm^{-1}$). Application of Student's t-test showed that, for this data set, there is a significant difference in the mean attenuation coefficient between ROIs containing intact myofibers (either from C57 or *mdx* mice) versus those containing necrotic lesions (from *mdx* mice) at the 1% significance level ($p < 0.01$). Conversely, for the small amount of data available, there is no significant difference ($p > 0.01$) in the attenuation coefficient between intact myofibers from healthy C57 mice versus those from dystrophic *mdx* mice.

## 4. Discussion

In this paper, we have quantified the attenuation coefficient $\mu_t$ of skeletal muscle tissue from healthy and, for the first time, dystrophic mice. We found that intact myofibers, whether from the healthy tissue of C57 mice or from the dystrophic tissue of *mdx* mice, had the lowest values of the attenuation coefficient (mean ± standard error): 3.9 ± 0.2 $mm^{-1}$ and 4.8 ± 0.3 $mm^{-1}$, respectively. In contrast, necrotic lesions from the dystrophic tissue of *mdx* mice, containing necrotic myofibers and infiltrating inflammatory cells, had the highest attenuation

#203628 - $15.00 USD Received 23 Jan 2014; revised 9 Mar 2014; accepted 11 Mar 2014; published 19 Mar 2014

coefficient: 9.6 ± 0.3 mm$^{-1}$. We also found that regions of dystrophic tissue of *mdx* mice in an intermediate state, containing fragmented necrotic myofibers but without the presence of infiltrating inflammatory cells, had an intermediate value of the attenuation coefficient: 7.0 ± 0.6 mm$^{-1}$. The measured attenuation coefficients should be system independent, as we have accounted for the modulation of the optical signal by the system confocal function of the focusing optics and coupling losses due to scanning.

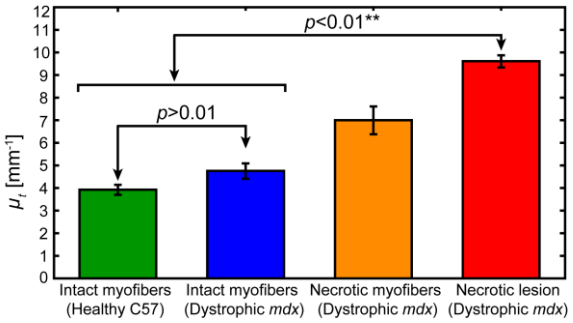


Fig. 6. Attenuation coefficients $\mu_t$ (mean ± standard error) of intact myofibers from C57 mice muscles (n = 10), intact myofibers from *mdx* mice muscles (n = 10), necrotic myofibers from *mdx* mice muscles (n = 2), and necrotic lesions from *mdx* mice muscles (n = 6), calculated from all muscle samples.

We cannot make a direct comparison of our results with those in the literature, as no values of $\mu_t$ measured at 1320 nm have been previously reported for skeletal muscle tissue. However, a number of papers show the wavelength dependence of the reduced scattering coefficient for mouse muscle, fitted to a power law relation of the form $\mu_s' = a\,(\lambda / 500\ nm)^b$, with the parameters $a$ and $b$ derived from fitting to empirical measurements made at lower wavelengths in the range ~400 – 900 nm. By extrapolating this model to $\lambda$ = 1320 nm, we can determine a range of the associated scattering coefficient by $\mu_s = \mu_s' / (1 - g)$ and assuming a reasonable range of anisotropy values for skeletal muscle tissue of $g$ = 0.94 – 0.97 [26]. Assuming scattering to be the major contributor to the total attenuation coefficient in skeletal muscle at this wavelength, we compare our values of extracted attenuation coefficient $\mu_t$ to values of the scattering coefficient $\mu_s$ indirectly obtained from the literature. Hall et al., measured 200 µm-thick slices of fixed mouse muscle tissue [27], giving $\mu_s$ = 5.0 – 10.1 mm$^{-1}$. From parameters specified in a review paper by Bashkatov et al. [28]: values were lower for 32 unfrozen beef muscle samples obtained from different animals $\mu_s$ = 4.0 – 8.0 mm$^{-1}$ [29]; a 1 mm-thick slice of superficial rat femoral muscle tissue gave $\mu_s$ = 5.6 mm$^{-1}$ at an associated anisotropy of $g$ = 0.93 [30]; whilst a single sample of fresh (unfixed) human abdominal muscle (mounted with the myofibers perpendicular to the direction of illumination) yielded higher values of $\mu_s$ = 7.0 – 14.0 mm$^{-1}$ [31]. From a more recent review by Jacques [32], two sets of parameters associated with muscle tissue from two different references are provided: the first gives values in the range $\mu_s$ = 8.8 – 17.6 mm$^{-1}$; whilst the second gives significantly lower values in the range of $\mu_s$ = 1.6 – 2.1 mm$^{-1}$. Given the variation of tissue sources and their respective preparation, the dissimilarity in the extrapolated value for the scattering coefficient $\mu_s$ at 1320 nm is not surprising and reflects the relative immaturity of the field of tissue optics, notwithstanding its apparent longevity. Since the values of the attenuation coefficient $\mu_t$ (3.9 ± 0.2; 4.8 ± 0.3; 7.0 ± 0.6; and 9.6 ± 0.3 mm$^{-1}$) from the muscle tissue compositions identified in this paper lie within the range of values of the scattering coefficient $\mu_s$ indirectly obtained from various samples of muscle tissue referenced in the literature, we are able to conclude from this comparison only that our results appear to be reasonable.

We expect the attenuation coefficient of necrotic lesions with infiltrating mononucleated inflammatory cells (9.6 ± 0.3 mm$^{-1}$) to be higher than regions of intact (non-necrotic)

#203628 - $15.00 USD Received 23 Jan 2014; revised 9 Mar 2014; accepted 11 Mar 2014; published 19 Mar 2014

myofibers, whether these are healthy myofibers (with peripheral nuclei) of C57 mice or regenerated myofibers (with central nuclei) of dystrophic *mdx* mice ($3.9 \pm 0.2$ mm$^{-1}$ and $4.8 \pm 0.3$ mm$^{-1}$, respectively). Necrotic lesions show an increased cell and organelle density, particularly the nuclei of infiltrating inflammatory cells, which contributes to increased scattering. Our results are consistent with those seen in samples of human lymph node associated with breast cancer, in which necrotic tissue had an attenuation coefficient of $\mu_t$ = ~$13.4 \pm 0.4$ mm$^{-1}$ (measured using OCT at 1320 nm) that was consistently higher than normal, non-fibrous tissue that ranged from $\mu_t = 4.5 - 11.5$ mm$^{-1}$. In this case, increased scattering was attributed to an increase in cell and organelle density as a result of the presence of metastatic deposits [22]. Similarly, human arteries with atherosclerotic plaques have shown higher attenuation coefficients for areas containing a necrotic core $\mu_t > 10$ mm$^{-1}$ or macrophage infiltration $\mu_t > 12$ mm$^{-1}$, compared with healthy vessel wall $\mu_t = 2 - 5$ mm$^{-1}$ (measured using OCT at 1310 nm) [20].

An explanation for the increased attenuation coefficient $\mu_t$ in necrotic lesions compared to regions of intact myofibers is an increase in the nuclei density. This can be clearly seen by comparing Fig. 3(d) and 3(a), respectively, and also Fig. 4(g) and 4(d), respectively. Cell nuclei contribute to high refractive index variations in tissue and are therefore a significant source of backscattering [33]. Thus, as the nuclei-to-cytoplasm ratio increases, as is the case for necrotic lesions with an abundance of infiltrating inflammatory cells, backscattering of the incident beam increases, leading to higher extinction and an associated increase in the attenuation coefficient.

A natural extension to this study is to increase the total number of samples of each tissue composition to accurately determine sensitivity and specificity of the identification of tissue type. In addition, *in vivo* measurements could be performed using miniature probes incorporated into needles to increase access to deep tissues [34–36]. The data acquisition rate would be improved by using a spectral-domain OCT system with greater scan speeds, which would be necessary for *in vivo* measurements. The analysis to extract $\mu_t$ from the large 3D data sets could be made more efficient by implementing the processing as a parallel algorithm, and determination of the spatially localized attenuation coefficient using depth-resolved analysis methods [37] could also aid in the 3D identification of necrotic lesions.

## 5. Conclusion

This paper presents quantitative parametric maps of the attenuation coefficient $\mu_t$ of *ex vivo* samples of healthy and dystrophic skeletal muscle tissue from a mouse model of muscular dystrophy. We applied this method to regions of muscle samples containing predominantly intact myofibers or necrotic myofibers with inflammatory cells, and found that the attenuation coefficient increases with increasing pathology. *En face* parametric maps of $\mu_t(x,y)$ were shown to improve the contrast of different tissue compositions, to aid in identification of necrotic lesions and to quantitatively assess the muscle. This analysis is based on quantification of intrinsic tissue attenuation, and is transferable between samples, experiments and systems. This technique improves on the contrast available in 3D OCT imaging of skeletal muscle and is a step towards *in vivo* assessment with OCT of mouse models of muscular dystrophy.

## Acknowledgments

The authors gratefully acknowledge the facilities and technical assistance of: CELLCentral; and the Centre for Microscopy, Characterisation & Analysis, a facility funded by the University, State and Commonwealth Governments; both at The University of Western Australia. We also thank colleagues Peter Munro and Peijun Gong for helpful discussions on the optical properties of tissue.

#203628 - $15.00 USD Received 23 Jan 2014; revised 9 Mar 2014; accepted 11 Mar 2014; published 19 Mar 2014